NREL
NATIONAL RENEWABLE ENERGY LABORATORY

Inflow Characterization and Aerodynamics Measurements on a SWT-2.3-101 Wind Turbine

Preprint

P. Medina and M. Singh
Siemens Energy, Inc.

J. Johansen and A. Jove
Siemens Wind Power A/S

L. Fingersh and S. Schreck
National Renewable Energy Laboratory

To be presented at the 50th AIAA Aerospace Sciences Meeting/Wind Energy Symposium
Nashville, Tennessee
January 9-12, 2012

NREL is a national laboratory of the U.S. Department of Energy, Office of Energy Efficiency & Renewable Energy, operated by the Alliance for Sustainable Energy, LLC.

Conference Paper
NREL/CP-5000-53666
January 2012

Contract No. DE-AC36-08GO28308

NOTICE

Available electronically at http://www.osti.gov/bridge

Available for a processing fee to U.S. Department of Energy
and its contractors, in paper, from:

U.S. Department of Energy
Office of Scientific and Technical Information

P.O. Box 62
Oak Ridge, TN 37831-0062
phone: 865.576.8401
fax: 865.576.5728
email: mailto:reports@adonis.osti.gov

Available for sale to the public, in paper, from:

U.S. Department of Commerce
National Technical Information Service
5285 Port Royal Road
Springfield, VA 22161
phone: 800.553.6847
fax: 703.605.6900
email: orders@ntis.fedworld.gov
online ordering: http://www.ntis.gov/help/ordermethods.aspx

Cover Photos: (left to right) PIX 16416, PIX 17423, PIX 16560, PIX 17613, PIX 17436, PIX 17721

Printed on paper containing at least 50% wastepaper, including 10% post consumer waste.

Inflow Characterization and Aerodynamic Measurements on a SWT-2.3-101 Wind Turbine

Paul Medina and Manjinder Singh,
Siemens Energy Inc., Boulder, CO, USA

Jeppe Johansen and Anna Rivera Jové
Siemens Wind Power A/S, Taastrup, Denmark

Lee Fingersh and Scott Schreck
National Renewable Energy Lab, Golden, CO, USA

Post processing techniques for aerodynamic data acquired from a Siemens' SWT-2.3-101 turbine have been developed and applied in this paper. The turbine is installed at the National Wind Technology Center (NWTC) as part of Cooperative Research and Development Agreement between Siemens Wind Power and the National Renewable Energy Laboratory (NREL) under U.S. Department of Energy (DOE) sponsorship. The results indicate that the use of these corrections is essential for accurate analysis of the data. An example of local inflow angles, velocities, and inflow velocity over the rotor plane derived from measurements from a 5-hole probe is also presented. Finally, the pressure measurements are used to characterize unsteady phenomenon, namely, rotational augmentation and dynamic stall on an inboard station. The results show that the rotational augmentation can considerably increase the attached flow regime compared to the 2D Computational Fluid Dynamics (CFD) results. The dynamic stall event was seen to significantly delay the stall. Furthermore, the non-dimensionalized vortex convection derived from the dynamic stall event was found to agree well with results from others studies.

I. Introduction and Background

Over the last few decades the trend of the wind industry has been for larger turbines capable of producing power at multi-megawatt levels using rotor diameters 100+ meters. Furthermore, increased focus on offshore development has led to even larger rotor diameters to reduce the total cost of energy produced. As a result, new rotor designs are driven to improve aerodynamic performance to maximize the energy captured while minimizing the loads acting on the blades. However, with larger rotor diameters, an additional design challenge must be addressed due to the ability of the rotor to interact with large energetic turbulent structures in the atmospheric boundary layer (ABL). Additionally, other features of the inflow, like high shear and yaw errors, have the potential to effect the performance of the rotor. Thus, for higher reliability, blade performance must be characterized for a wide and highly dynamic range of parameters over which the turbine can be anticipated to operate.

To provide a test bed for such a characterization, Siemens Wind Power and the National Renewable Energy Laboratory (NREL) entered into a Cooperative Research and Development Agreement (CRADA) in December 2008. Under this agreement, a Siemens 2.3 MW turbine was installed on the National Wind Technology Center (NWTC) grounds in Golden, Colorado, to support numerous research activities that will result in improved understanding of wind turbine rotor-dynamics and provide high quality data that will lead to better and more efficient rotor designs. The site is particularly suitable for this study because of its extreme wind conditions, with strong shear, high turbulence intensity, severe wind ramps, and gust events. The test turbine erected under the CRADA agreement is a Siemens SWT-2.3-101 turbine. It is a pitch-regulated variable-speed turbine with a rated power of 2.3 MW and a rotor diameter of 101m. The tower height is 80m and the 49m long blades are designed specifically for reducing loads and increasing power at moderate wind speeds. The blades are made of fiberglass reinforced epoxy using a Siemens' proprietary manufacturing process. The turbine is designed to run between wind speeds of 4 and 25 m/s, with nominal power being reached at 12 to 13 m/s. The rotor speed varies between 6 and 16 rpm.

A wide range of research studies are being conducted under the CRADA, a good overview of which can

be found in reference 1. The focus of the work presented in this paper is to (1) demonstrate the development and implementation of data reduction algorithms for the measured pressures, (2) demonstrate an example for use of a five hole probe to obtain local inflow velocities and angles, and (3) demonstrate the use of data being collected for studying features like rotational augmentation and dynamic stall that are most likely to influence the blade performance on inboard sections. The overall objective of these tests is to develop a broad database that can be used for validation and improvement of the tools that are used in the blade design cycle.

II. Data Acquisition and Analysis

A. Inflow Measurements

Most of the aerodynamic data presented in this paper was characterized from a 80m tower approximately 2.5 rotor diameters (D) upwind of the turbine. This tower is instrumented with one sonic anemometer, four levels of cup anemometers and directional vanes, two levels of temperature, and barometric pressure. For this project, turbine hub height instrumentation is IEC-class. This includes a class-1 cup at 80m, another at 78.5m along with a vane at that level, and a barometric pressure sensor and temperature sensor just below that. The data acquisition system runs continuously at 20 Hz. Due to the need to accurately characterize the ABL, as well as the inflow across the turbine rotor, a 135m meteorological tower was installed approximately 2 rotor diameters away from the turbine in the dominant wind direction and will be used for future measurements. The 135m tower consists of six levels of cup anemometers and directional vanes, six levels of sonics with 3-axis accelerometers, four levels of temperature, a barometric pressure sensor and a precipitation sensor. All of these sensors are placed at different heights between 3 and 134m from the ground.

Additionally, in collaboration with University of Colorado, Boulder, a portable NRG System's Windcube LIDAR has been installed on-site approximately 2.8 rotor diameters upstream of the turbine in the dominant wind direction to characterize the inflow. The LIDAR is capable of measuring three velocity components (between 0 to 60 m/s) within a 40 to 200m range, with scanning cone angle of 15° and 30°. Though the system is capable of producing high temporal resolution data, currently it is being used to acquire averaged data (over 10 minutes) at 40, 50, 60, 80, 100, 120, 140, 160, 180, and 200m above the ground.

B. Pressure Measurements

To obtain useful surface pressure data, one of the blades is extensively instrumented to provide the pressure measurements at nine span-wise locations. Each of the nine span-wise locations has approximately 60 to 64 pressure taps, distributed based on expected pressure distributions, that provide sufficient resolution to develop reliable models and CFD comparisons. Figure 1 depicts the span-wise locations used on the blade for pressure measurements and 5-hole probes. The pressure at each of these stations is acquired using a combination of ZOC33 and ERAD-4000 modules, from Scanivalve Corporation, at 25 Hz and is transmitted wirelessly to a remote computer for storage and post-processing. To avoid the sensor drifts due to variation in temperature, the pressure modules are housed in a temperature control unit (TCU) that maintains the temperature of the modules at ≈ 25°C. Additionally, to reduce the maximum rotational acceleration of the

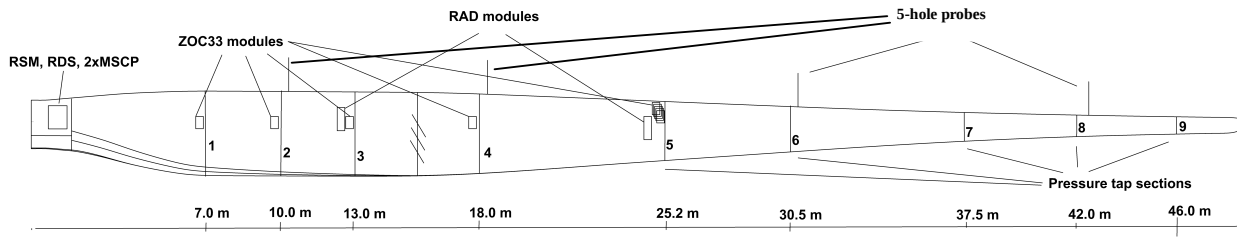

Figure 1. Schematic of the instrumented blade showing the locations of measurements stations and 5-hole probes.

pressure sensors, all the instruments are mounted inside of 25m blade radius and aligned appropriately as suggested by the manufacturer. Furthermore, four 5-hole probes also shown in Figure 1 are installed to measure local inflow angles and velocities. These probes extend approximately 0.6m ahead of the blade leading edge. The setup for data acquisition is essentially the same as was described for the pressure measurements.

C. Post-Processing: Data Corrections

Past studies[2,3] have shown that certain physical phenomenon manifest themselves on the actual pressure distribution and must be accounted for in the pressure measurements conducted on a turbine. While most of these corrections are well understood and have been successfully implemented in the past studies, the nature of the measurements being conducted here also requires an additional correction that has not been previously used on turbine-scale experiments. The following discussion provides a brief description of the corrections that are used in this study.

1. Pressure correction for the tubing effect

In the current setup the pressure measurements are conducted remotely. The sensors are not flush with the surface but are connected to the surface ports through long pressure tubing of varying geometry. In such cases, the tubing affects the pressure measurements in a manner similar to a low pass filter by attenuating the amplitude and introducing a phase shift as compared to the original signal.[4] The tubing correction is used to determine a transfer function that removes this attenuation and phase shift. The mathematical development of this correction is quite intensive and can be found in the work by Strike et al.[4]

Depending on the measurement station, the tubing configuration changes (see Figure 1). The worst case scenario (that produces the most amplitude attenuation and phase shift between measured and actual signal) is expected at station 9, which uses the longest tubes, in three different diameters. Thus, wind tunnel tests for validating the tubing effect correction were conducted by exactly replicating the tubing layout used for station 9. The tubing system was installed on a pitching airfoil, which also had a surface mounted transducer for validating the reconstructed signal. Figure 2 (a) shows results from one such test in which the airfoil was

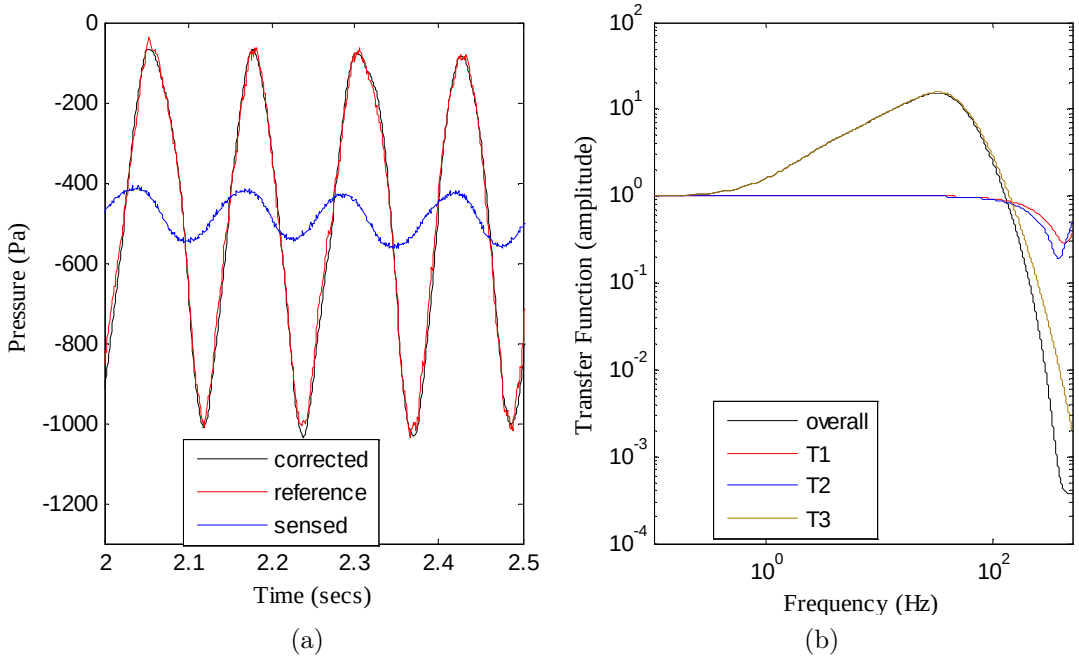

Figure 2. (a) Validation measurements for the tubing corrections using a pitch oscillating airfoil at 8 Hz.(b) Overall transfer function and its decomposition to show the individual contribution of the tubing used in cascaded connection.

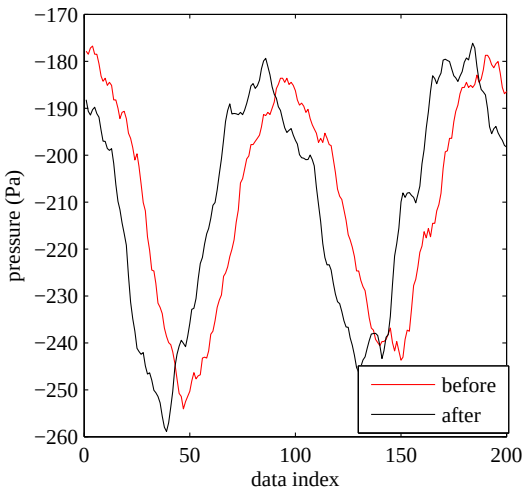

Figure 3. Application of the tubing correction on an arbitrarily selected time series from station 2.

oscillating at 8 Hz. As can be observed, the reconstructed signal almost exactly follows the reference signal (acquired by the surface mounted transducer). For the tubing correction, the transfer function calculation is based not only on the geometrical features of the tube, but also on the atmospheric pressure and ambient temperature at the time of measurements. The transfer function is then applied to the measured signal. The transfer function for station 9 used in this study is shown in Figure 2(b). Additionally, the individual contribution of each of the tubing (T1 - 1mm diameter 0.1m long, T2 - 1.6 mm diameter 0.2m long, and T3 - 3mm diameter 25.8m long) is also shown in this figure. As expected, most of the attenuation is due to the longest tubing in this system. To demonstrate that the tubing effect can be significant for smaller lengths of tubing also, Figure 3 shows a signal at arbitrary chord wise location on station 2, which uses 1.6mm diameter tubing 4.25m long and a 1mm diameter tubing 0.1m long. As the Figure depicts, even though the amplitude is not affected much by the smaller tubing, a significant phase shift still exists in the signal.

2. Hydrostatic correction

Consider Figure 4 that depicts the installation of differential transducers used for measurements. As the blade rotates, the transducer undergoes vertical translation. As a result, the transducer sees a hydrostatic pressure variation of approximately 10 Pa/m at the site. Since the transducer measures differential pressure differences, one would expect that this hydrostatic variation will not influence the transducer measurements. However, the presence of tubing on either side of the transducer introduces phase and amplitude shifts in hydrostatic pressure sensed by the transducer, due to same reasons that were discussed for the tubing correction. Thus, the sensed signal must be corrected to remove this effect. If, ψ is the azimuthal position of the rotor, r is the radial position of the transducer, w.r.t to hub center, and ρ the air density, then the hydrostatic correction, ΔP_{HS} , is given by,

$$\Delta P_{HS} = -A_{pr}\rho g r \cos(\psi - \phi_{pr}) - (-A_{ref}\rho g r \cos(\psi - \phi_{ref})). \tag{1}$$

Where, ϕ_{pr} and ϕ_{ref} represent the phase lag introduced by the tubing, and A_{pr} and A_{ref} represent the amplitude changes on the pressure and reference side of the transducer respectively. As expected, in the absence of tubing, $A_{pr} = A_{ref}$ and $\phi_{pr} = \phi_{ref}$ leading to $\Delta P_{HS} = 0$. However, the current measurement system uses a static basket with a slow leak. Due to this, for the current analysis, the latter term used to model the reference side of transducer is neglected. A_{pr} and A_{ref} were determined using the same theory as that used for the tubing correction. Figure 5 shows the effect of the hydrostatic correction on measured signal on station 2 (after correcting for tubing effect). The low frequency oscillations seen in the "before" signal corresponds to 1-p frequency. As the figure shows, the 1-p frequency content is largely removed by

taking into account the hydrostatic variation. The remaining fluctuation is attributed to variations in inflow conditions.

3. Reference pressure correction

As was mentioned previously, the reference side of the transducers is connected to a static basket located in the hub with a small leak. Additionally, the axial pressure variation based on the actuator disc model (see Figure 6) also predicts that the basket would not sense the freestream static pressure irrespective of the size

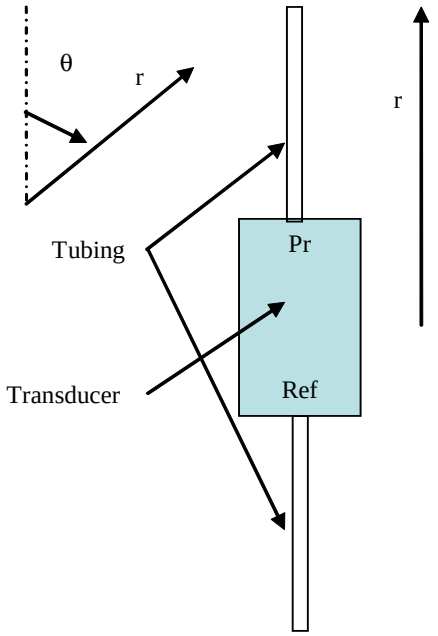

Figure 4. Schematic of the transducer used for development of the hydrostatic correction.

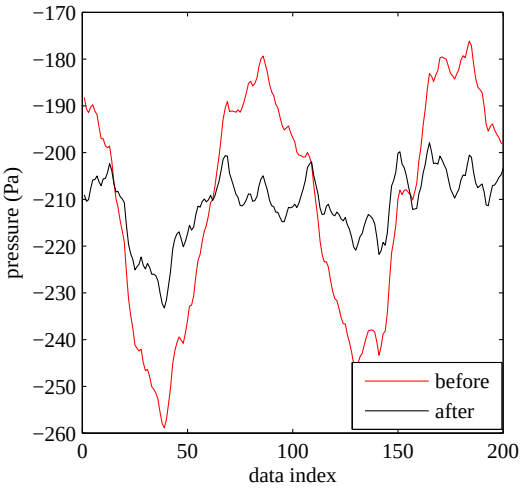

Figure 5. Application of hydrostatic correction on an arbitrarily selected time series on station 2. The "before" signal is corrected for the tubing effect.

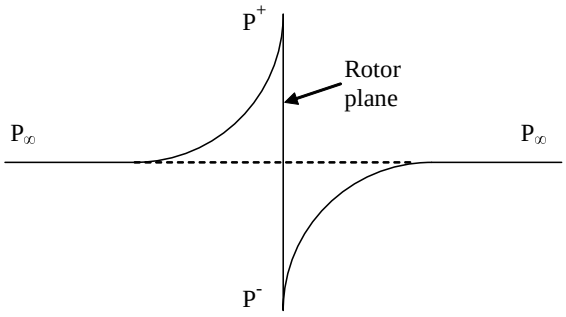

Figure 6. Axial pressure variation from actuator disc theory.

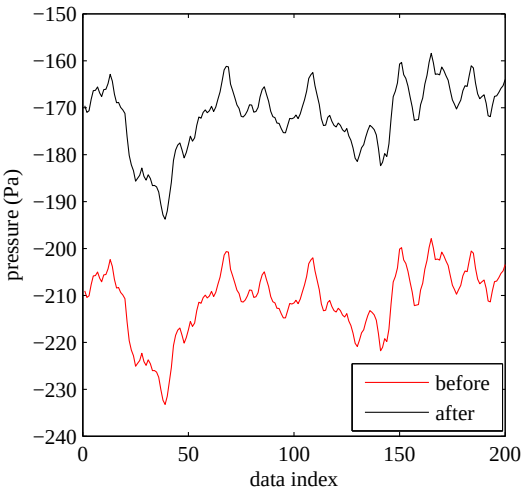

Figure 7. Application of reference pressure correction to an arbitrarily selected times series on station 2. The "before" signal is already corrected for tubing and hydrostatic effects.

of the leakage. Thus, the measured values are not actually referenced to the freestream static pressure, P_∞, but the pressure in static basket, P_{sb}. The measured signal must, therefore, be corrected to account for the error, $P_{ref} = P_\infty - P_{sb}$. From Bernoulli's theorem, the freestream total pressure can be written as

$$P_{atm} = Q_{met} + P_\infty \tag{2}$$

Where, Q_{met} is the dynamic pressure based on freestream velocity V_∞ measured at hub height. Furthermore, Bernoulli's theorem also allows to state that the absolute stagnation pressure (P_{stag}) as,

$$P_{stag} = P_{atm} = Q_{met} + P_\infty. \tag{3}$$

Also, since the measured pressure is w.r.t to the static basket, we have

$$P_{atm} = P_{stag,measured} + P_{sb}. \tag{4}$$

Where $P_{stag,measured}$ is the measured stagnation w.r.t. P_{sb} (recall that P_{stag} is an absolute quantity.) The correction can then be determined as,

$$\Delta P_{ref} = P_\infty - P_{sb} = P_{stag,measured} - Q_{met} \tag{5}$$

The corrected pressure is then computed as $P_{corrected} = P_{measured} - P_{ref}$. Experience has shown that a minimum of 2 minute data (25 sample/sec*120 sec = 3000 samples) is required to obtain a converged correction value. As an example Figure 7 shows an arbitrarily corrected sample using the above formulation. As the figure shows, the correction acts by offsetting the measured pressure.

4. Centrifugal Correction

Much like the hydrostatic correction, another phenomenon affects the pressure measurements as the blade rotates. This is due to the centrifugal force that the air trapped in the tubing exerts on the pressure and the reference side of the transducer. However, unlike the hydrostatic pressure, the centrifugal pressure acting on the transducer diaphragm depends on the speed of the rotor and not its azimuthal position. Figure 8 depicts the layout that will prove useful in developing the model for the centrifugal correction. In the figure, the pressure due to the centrifugal forces is shown at each tubing end. The unmarked side of the reference tubing terminates in the hub and does not experience any effect due to centrifugal pressure. These equations

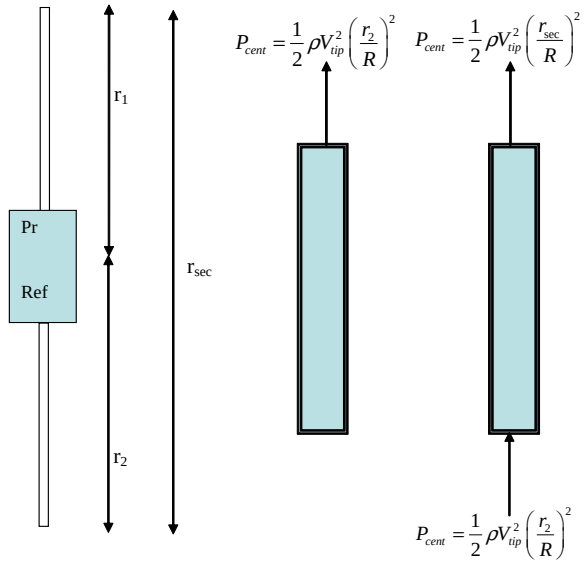

Figure 8. Schematic showing centrifugal pressure on pressure and reference side of the transducer.

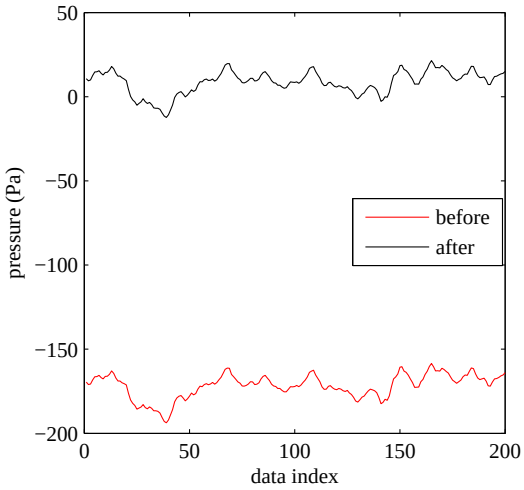

Figure 9. Application of the centrifugal correction to an arbitrarily selected signal on station 2. The "before" signal is already corrected for tubing, hydrostatic, and reference effects.

assume that the air density is not changing with height within the rotor diameter. These pressures can be combined to show that the centrifugal pressure correction is only a function of blade rotation speed and the location of the station at which the pressure is being measured and is given by,

$$\Delta P_{cent} = \frac{1}{2}\rho V_{tip}^2 \left(\frac{r_{sec}}{R}\right)^2 \tag{6}$$

Where, V_{tip} is the tip speed, R is the rotor radius, and r_{sec} is the radius of the measurement station for which the correction is being calculated. To demonstrate the effect of this correction, Figure 9 shows an arbitrarily selected signal at station 2 before and after applying the centrifugal correction. As the figure shows, centrifugal force is responsible for causing the most offset in the measured signal and, thus, is a critical quantity to account for while analyzing the results.

The pressure measurements from the surface ports are post-processed to remove these effects. However, for the pressure measurements from the 5-hole probes, in addition to the above mentioned corrections, a data reduction method technique is used to obtain the instantaneous inflow velocity, local inflow angle, and the local slip angle.

D. Inflow angle and velocity: 5-hole probes

To correctly identify the comparison points for the experimental and computational data, it is important to determine the correct inflow angle and velocity at which the data is acquired. The 5-hole probes that are mounted on the leading edge of the blade are one of the most direct methods to instantaneously determine the inflow angles and velocities the turbine blades are subjected to as they undergo rotation. In principle, such direct measurements eliminate the need to account (in post-processing) for turbulence, yaw, and shear in the flow. Figure 10 provides an example of the type of data before and after post-processing. The acquired pressures P1-6 are shown in the two figures in the first column and the variables obtained after post-processing (local inflow and slip angles and local velocity at the probe tip) are shown in the figures in the second column. The steps required to obtain the local inflow angles and velocities are standard and well understood. However, the measurements from a 5-hole probe on an blade are also susceptible to induced

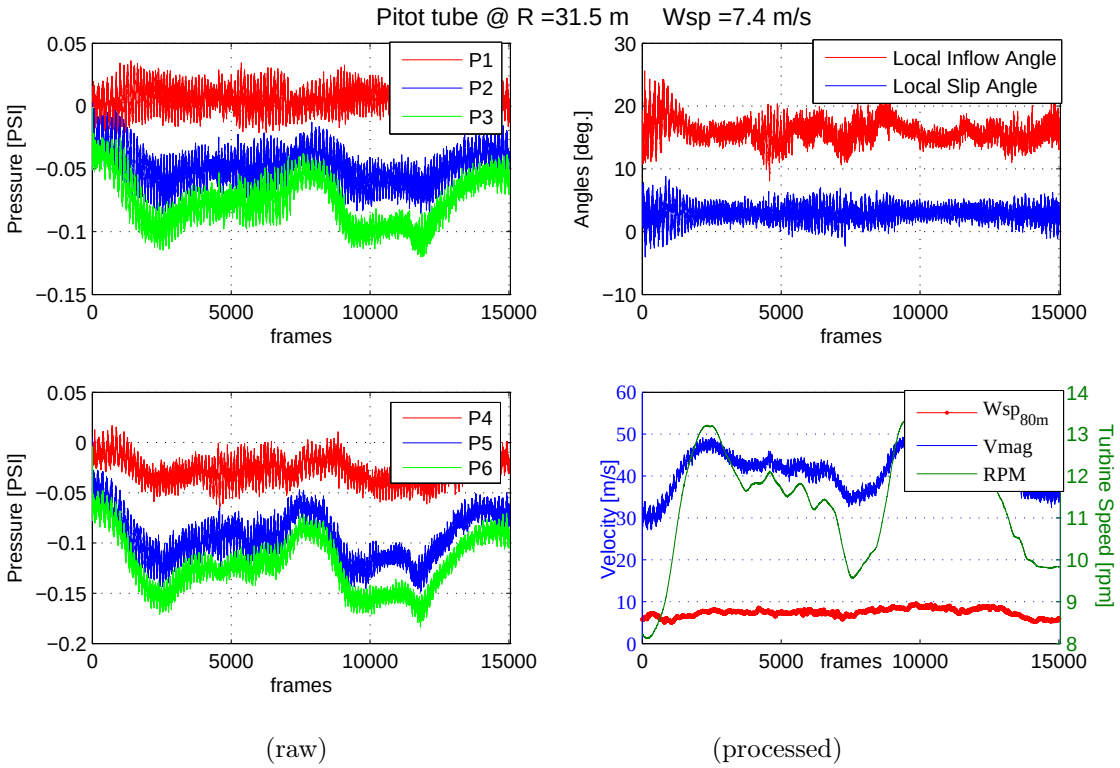

Figure 10. An example to demonstrate the data acquired and analyzed from 5-hole probes.

velocity due to bound circulation. The induced velocity leads to higher measured angles of attack at the probe tip and must be accounted for. This so called upwash correction requires extensive use of simulations and thus is very dependent on local blade profiles. The upwash correction, though has been implemented and tested, is beyond the scope of work presented here and is, thus, not discussed further.

III. Results and Discussion

The first step after collecting the measurements is to apply the corrections that were discussed in section IIC. These corrections remove the "artifact" effects caused by acquiring the data on a rotor in field. Figure 11 demonstrates an example of the C_p distribution resulting from acquisition, after corrections and also compares the results to the computed C_p from CFD. The gaps in the measured data are due to a filtering of channels showing bad data resulting from freeze, and plug. These frozen/plugged channels measure pressures very close to zero and are easily identified by observing the pressure distribution. In general, the experimental and CFD data are in better agreement at the outboard stations than at the inboard stations. This may be attributed to the inability of CFD tools to fully capture the complex flow physics associated with 3-D separated flows occurring near the root and behind flat back airfoils. It must be noted here that the pressure distributions on the inboard sections are more sensitive to the wind speed, and the 5% difference in the measured (21 m/s) and simulated wind speed (20 m/s) may have added to the noted disagreement on the inboard sections. Nonetheless, this is a perfect example that shows an application that can benefit from the data being collected in this campaign. On the outboard stations, CFD does a very good job of predicting the pressure distribution. Although not shown here, additional comparisons at other wind velocities also showed a similar agreement between post-processed pressure distributions and the predicted pressure distribution using CFD.

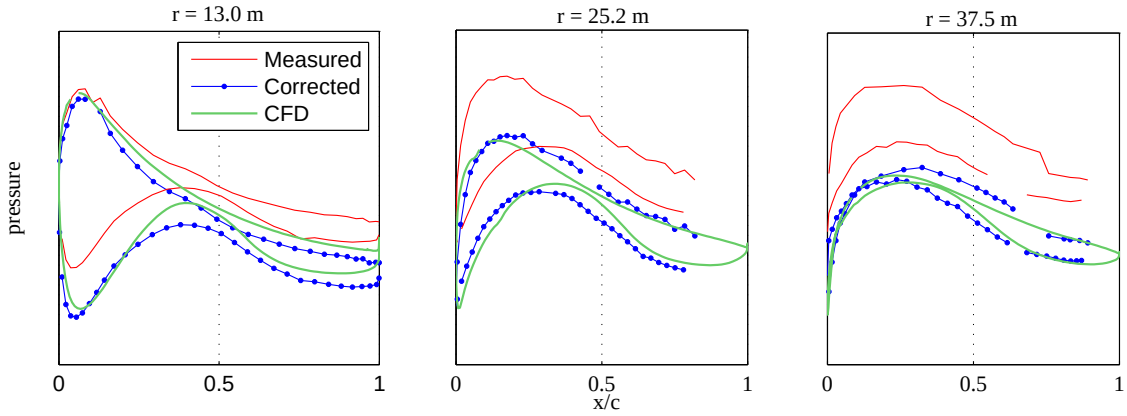

Figure 11. Comparison of a sample measurement that has been corrected with the CFD results at $V_\infty = 20$m/s at three stations. Scale on Y-axis has been removed due to confidentiality.

The corrected data shown in Figure 11 represent a relatively low angle of attack, steady blade operating state, in which separation and unsteadiness exercised negligible effects. However, turbine testing also captured periods wherein separation and dynamic effects were prominent, as in rotational or dynamic stall. Occurrences typifying these two phenomena are documented below.

A. Inflow profile from 5-hole probes

The derivation of local inflow angles and speed from 5-hole probes was discussed earlier. In addition to these parameters, the data acquired from a 5-hole probes can also be used to derive inflow profiles. As the blade undergoes a full rotation, the most outboard probe (at $r = 43$m) provides an envelope that covers most of the area swept by the rotor. Thus, the useability of the inflow velocity at the probe tip can be extended by creating a inflow profile. For example, Figure 12 shows a inflow profile (averaged over 10-minutes) obtained from the 5-hole probe measurements that have been binned based on the blade azimuthal position during the downstroke (U_1) and upstroke (U_2). The figure also shows the mean profile (U_mean) from measurements and those from a 135m met tower and a Lidar. The calculation of incoming velocity profile is essentially

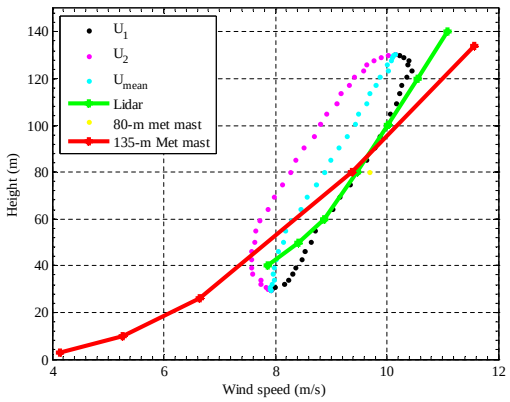

Figure 12. Estimation of inflow profile using 5-hole probe located at 43m radius. U_1 represents the measurement during downstroke and U_2 represents the measurements during the upstroke. U_{mean} is the mean velocity from U_1 and U_2.

derived by interpolating the correlation between the wind speed at the probe tip and the freestream velocity. This correlation was obtained using a Siemens in-house aeroelastic design code. As the figure shows, the measurements obtained from the probe provide a very good estimate of shear in the incoming flow. The difference in the profiles during the upstroke and downstroke can be attributed to the yaw error. Nonetheless, the mean profile shows a good match to the meteorological tower and Lidar data with acceptable accuracy.

B. Rotational Augmentation

To isolate and analyze rotational augmentation, inflow conditions were identified during which wind speed and direction varied to a minimal degree. This results in low yaw error turbine operation approximating an axisymmetric flow state. Under these conditions, surface pressure distributions consistent with a rotationally augmented flow field were observed. Representative suction surface C_p distributions (obtained by normalizing the pressure distribution with maximum pressure assumed to be the stagnation pressure) acquired on November 23, 2011, during 2040 - 2050 hrs (MST), at the 11.3 m radius location are shown in Figure 13, and correspond to cycle 50 of the 10 minute data set.

In Figure 13, C_p distributions are shown for rotor azimuths of 0°, 90°, 180°, 270°, and 360°. Analysis showed that the angle of attack during this time was approximately 24°. Minimum C_p values were recorded at

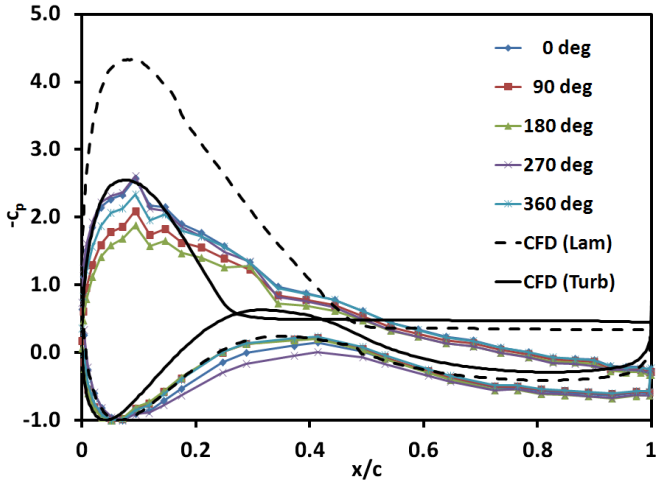

Figure 13. Typical rotational augmentation suction surface C_p histories, at the 11.3m radial station.

x/c = 0.094, and ranged from -1.9 to -2.6 for the five rotor azimuths. A predominantly linear C_p distribution having a moderate adverse gradient was present over $0.094 \leq x/c \leq 0.344$, and over $0.344 \leq x/c \leq 1.00$ was supplanted by a similarly pseudo-linear C_p distribution, though of decreased gradient. The strongly linear character is reminiscent of the C_p distributions observed by Ronsten,[5] but differs from the C_p distributions documented for the UAE Phase VI and MEXICO experiments.[6]

To establish a baseline for the current measurements, which included three-dimensionality and rotation, computations were carried out for the $r = 11.3$m blade section under two-dimensional, non-rotating conditions. The computational results were obtained from steady RANS (Reynolds Averaged Navier-Stokes equations) using the SST (Shear Stress Transport) turbulence model. The results are shown in Figure 13, for laminar and fully turbulent boundary layers.

The laminar boundary layer computations deviate substantially from the measured data and apparently offer little insight into the rotational augmentation flow physics. However, for most rotor azimuths, the turbulent boundary layer predictions generally agree with the measurements over the forward part of the chord ($x/c < 0.175$). In contrast, aft of x/c = 0.175, the computational predictions and the measured data all deviate widely. The most notable difference between the two is the absence of pressure recovery aft of $x/c = 0.25$ for the computational surface pressures, and the persistence of an appreciable surface pressure gradient over the same chord region in the measured data. This distinction credibly confirms the augmenting influence of rotational effects on the boundary layer and the resulting effect of delaying or precluding separation.

C. Dynamic Stall

Blade suction surface C_p distributions were examined to clarify the physics of the vortex dominated flow field via detection and tracking of the dynamic stall vortex. Blade C_p histories are shown in Figure 14, which were acquired, on May 5, 2011 during 2030 - 2040 hrs (MST), at the 11.3m rotor radial station. It must be noted here that this event was captured while the turbine operated in off-design conditions/parameters that were selected specifically to enable capturing of such data. The data shown in Figure 14 correspond to cycle 100 of the 10 minute data set, and were typical of dynamic stall episodes observed in the database. During cycle 100, average local inflow speed (U_{loc}) at the 11.3m radius location was 19.0 m/s. Using this inflow speed along with local blade chord (c) and rotor rotation rate (Ω) yielded a reduced frequency $K = 0.095$ ($K = c\Omega/2U_{loc}$).

Figure 14 contains 13 suction surface C_p histories plotted versus rotor azimuth angle (ψ). $\psi = 240^\circ$ corresponds to the 12 o'clock position for the pressure tapped blade, and the blade rotates clockwise as viewed from upwind. Trace 1 at the bottom of the panel corresponds to the leading edge pressure tap, with successively higher traces corresponding to tap locations progressively farther aft on the suction surface blade chord. Traces are tagged with blade chord location (x/c) near the right border of the plot. Surface pressure minima corresponding to dynamic stall vortex presence[7,8] have been highlighted with a filled circle symbol.

In Figure 14 soon after $\Psi = 0^\circ$, C_p began to decrease at all 13 taps, first at tap locations near the leading edge and shortly thereafter at tap locations farther aft. Decreasing surface pressures culminated in well defined C_p minima corresponding to dynamic stall vortex presence and marked by filled circles. After C_p minima were attained, surface pressures again increased, signaling departure of the dynamic stall vortex. These C_p minima occurred at later times for taps farther aft on the blade chord, consistent with a dynamic stall vortex that initiated near the leading edge, and then convected aft toward the trailing edge. At $x/c = 0.34$, C_p time variation yielded troughs that were deep and narrow, indicating passage of a condensed vortex structure. By the time the dynamic stall vortex reached the trailing edge, deep, narrow C_p troughs had been supplanted by broader, shallower C_p depressions, indicating alteration to the vortex structure, and passage of a more expansive vortex structure.

When present, the dynamic stall vortex dominated the flow field over the blade. To better comprehend the physics of the vortex and the influences it exercised on the blade aerodynamics, the kinematics of the dynamic stall vortex were documented in further detail. Dynamic stall vortex convection history was extracted from Figure 14. This showed that the dynamic stall vortex convected from the leading edge vicinity toward the trailing edge with only minor deviations from constant speed. A linear least squares fit was applied to the vortex convection history to obtain the average chordwise convection speed. Nondimensionalizing average vortex convection speed (V_{dsv}) with respect to the local inflow speed (U_{loc}) showed that V_{dsv} was 22 percent of U_{loc}. This value of V_{dsv}/U_{loc} was consistent with observations reported for the UAE Phase IV field test[9] and for oscillating airfoil experiments in the Ohio State University wind tunnel.[10]

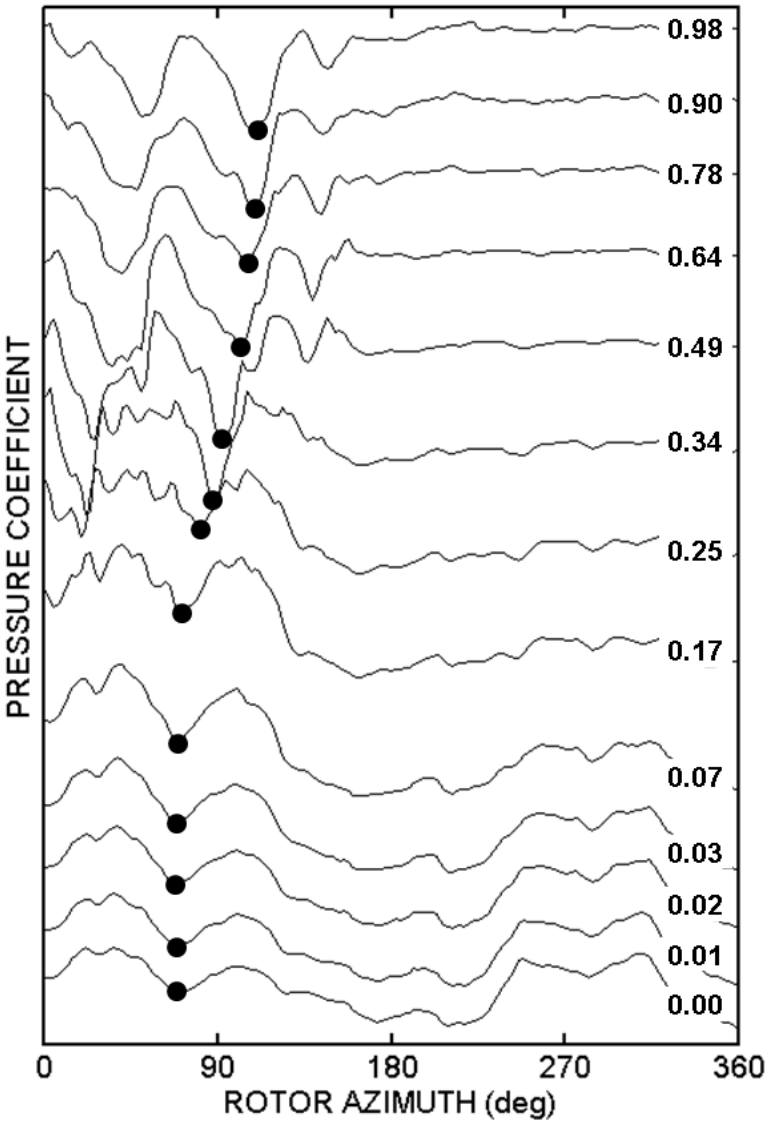

Figure 14. Typical dynamic stall suction surface C_p histories, at the 11.3 m radial station. The traces have been offset vertically to facilitate viewing and zero references have been omitted.

IV. Conclusions

Aerodynamic data acquired on a Siemens' 2.3-101 turbine were analyzed to (1) develop and demonstrate post processing method, (2) demonstrate the use of 5-hole probe data for obtaining local inflow velocity, angles, and (3) confirm the detection of dynamic stall and rotational augmentation events. The acquired data are corrected to remove effects of four phenomena, namely, the filtering effect of the tubing, the hydrostatic pressure variation, the reference pressure, and the centrifugal effects. While the first two corrections provide the correct amplitude and phase, the latter corrections help by removing the temporal offsets from the signal that result from the rotation of the blades. The results indicate that all of these corrections are essential for improving the accuracy and quality of data analysis. The 5-hole probes provide instantaneous local inflow velocities and angles, which are useful for comparing the actual forces from the blade cross-sections to those obtained from CFD. Use of 5-hole probe data for deriving the inflow to rotor has also been explored.

Rotational augmentation and dynamic stall that result from wind unsteadiness and high angles of attack have also been studied. Compared to the 2D CFD results at r = 11.3m, which showed that almost 75% of the airfoil stalled at 24°, the measured pressure did not show any separation. These results indicate that on the inboard station covered in this work, separation, and thus, the stall angle is delayed significantly due to

rotational augmentation. The vortex convection rate calculated from a dynamic stall event captured during high winds was found to agree well with other studies.

Data and analysis in the current work show that the Siemens SWT-2.3-101 turbine sited at the NWTC is capable of furnishing research grade rotor aerodynamics measurements. In the recently initiated phase of the project, blade aerodynamic measurements will be complemented with high quality inflow data from a 135m meteorological tower. In subsequent work, blade aerodynamics and meteorological tower inflow data will be correlated to further clarify rotor and inflow fluid dynamic phenomena responsible for the spectrum of aerodynamic loads produced by multi-megawatt turbines. Clear understanding and accurate prediction of these loads will enable turbines that are more aerodynamically efficient and structurally reliable, which will facilitate continued reductions in the cost of wind energy.

Acknowledgements

The authors would like to acknowledge the contributions of Ewan Machefaux, (graduate student from Technical University of Denmark, past intern at Siemens Wind Power) for implementing the programs used for post-processing of the data presented in this paper. The authors also gratefully acknowledge the support of the Department of Energy Wind and Water Program Office under the contract CRD-08-303.

References

[1]Medina, P., Singh, M., Johansen, J., Jové, A. R., Machefaux, E., Fingersh, L., and Schreck, S., "Aerodynamic and Performance Measurements on a SWT-2.3-101 Wind turbine," *AWEA Windpower Conference and Exhibition*, Anaheim, CA, May 22-25 2011.

[2]Hand, M. M., Simms, D. A., Fingersh, L. J., Jager, D. W., Cotrell, J. R., Schreck, S., and Larwood, S. M., "Unsteady Aerodynamics Experiment Phase VI: Wind Tunnel Test Configurations and Available Data Campaigns," Tech. Rep. NREL/TP-500-29955, NREL, 2001.

[3]Madsen, H. A., Bak, C., Paulsen, U., Gaunaa, M., Fuglsang, P., Romblad, J., Olesen, N. A., Enevoldsen, P., Laursen, J., and Jensen, L., "The DAN-AERO MW Experiments, Final report," Tech. Rep. Risø-R-1726(EN), Risø, 2010.

[4]Strike, J. A., Hind, M. D., Saini, M. S., and Naughton, J. W., "Unsteady Surface Pressure Reconstruction on an Oscillating Airfoil Using the Wiener Deconvolution Method," *27th AIAA Aerodynamic Measurement Technology and Ground Testing Conference*, No. AIAA 2010-4799, 28th June - 1st July, Chicago, Illinois., 2010.

[5]Ronsten, G., "Static pressure measurements on a rotating and a non-rotating 2.375 m wind turbine blade: comparison with 2D calculations," *J. of Wind Engineering and Industrial Aerodynamics*, Vol. 39, 1992, pp. 105–118.

[6]Schreck, S., Sant, T., and Micallef, D., "Rotational Augmentation Disparities in the MEXICO and UAE Phase VI Experiments," *Proceedings of the 2010 Torque from Wind Conference*, June, 2010.

[7]Walker, J., Helin, H., and Strickland, J., "An Experimental Investigation of an Airfoil Undergoing Large Amplitude Pitching Motions," *AIAA 23rd Aerospace Sciences Meeting*, No. 85-0039, 1985.

[8]Schreck, S., Addington, G., and Luttges, M., "Flow Field Structure and Development Near the Root of a Straight Wing Pitching at Constant Rate," *AIAA 22nd Fluid Dynamics, Plasma Dynamics and Lasers Conference*, No. 91-1793, Jun, 1991.

[9]Schreck, S., Robinson, M., Hand, M., and Simms, D., "HAWT Dynamic Stall Response Asymmetries Under Yawed Flow Conditions," *AIAA Aerospace Sciences Meeting*, No. 2000-0040, Jan, 2000.

[10]Ramsay, R. R., Hoffman, M., and Gregorek, G., "Effects of Grit Roughness and Pitch Oscillations on the S809 Airfoil," Tech. Rep. NREL/TP 442-7817, NREL, Golden, CO, 1995.